# High pixel number deformable mirror concept utilizing piezoelectric hysteresis for stable shape configurations

Huisman, Robert; Bruijn, Marcel P.; Damerio, Silvia; Eggens, Martin; Kazmi, Syed N.R.; Schmerbauch, Anja; Smit, Heino; Vasquez Beltran, Marco; van der Veer, Ewout; Acuautla, Mónica

*Published in:*
Journal of astronomical telescopes instruments and systems

*DOI:*
10.1117/1.JATIS.7.2.029002



*Publication date:*
2021

# High pixel number deformable mirror concept utilizing piezoelectric hysteresis for stable shape configurations

**Robert Huisman**[a,*] **Marcel P. Bruijn**[a] **Silvia Damerio**[b] **Martin Eggens**[a] **Syed N. R. Kazmi**[a] **Anja E. M. Schmerbauch**[c] **Heino Smit**[a] **Marco Augusto Vasquez-Beltran**[c] **Ewout van der Veer**[b] **Mónica Acuautla**[c] **Bayu Jayawardhana**[c] **and Beatriz Noheda**[b]

[a]SRON Netherlands Institute for Space Research, Groningen, The Netherlands
[b]University of Groningen, Zernike Institute for Advanced Materials, Groningen, The Netherlands
[c]University of Groningen, Engineering and Technology Institute of Groningen, Groningen, The Netherlands

**Abstract.** We present the conceptual design and initial development of the hysteretic deformable mirror (HDM). The HDM is a completely new approach to the design and operation of deformable mirrors (DMs) for wavefront correction in advanced imaging systems. The key technology breakthrough is the application of highly hysteretic piezoelectric material in combination with a simple electrode layout to efficiently define single actuator pixels. The set-and-forget nature of the HDM, which is based on the large remnant deformation of the newly developed piezomaterial, facilitates the use of time division multiplexing to address the single pixels without the need for high update frequencies to avoid pixel drift. This, in combination with the simple electrode layout, paves the way for upscaling to extremely high pixel numbers ($\geq 128 \times 128$) and pixel density ($100/\text{mm}^2$) DMs, which is of great importance for high spatial frequency wavefront correction in some of the most advanced imaging systems in the world. © *2021 Society of Photo-Optical Instrumentation Engineers (SPIE)* [DOI: 10.1117/1.JATIS.7.2.029002]

**Keywords:** deformable mirror; hysteretic piezomaterial; set-and-forget actuator; time division multiplexing; high pixel count; space instrumentation.

Paper 20185 received Dec. 21, 2020; accepted for publication Apr. 1, 2021; published online Apr. 23, 2021.

## 1 Introduction

The search for planets outside our solar system (so-called exoplanets) experienced a great boost after the discovery of the first exoplanets in the 1990's. Since then, already more than 4000 exoplanets have been found with mostly indirect detection techniques, such as the transit method and the radial velocity method.[1] These techniques do not collect the light from the very faint planet itself but observe the effect it has on its accompanying star. Although these techniques are very suitable to discover exoplanets, they do not provide information about the chemical composition of a possible atmosphere surrounding the planet and thus about the possibility of life existing on this planet. If the orbit of the planet is such that its path crosses the line of sight of the telescope to the host star, one can observe the changes in the spectrum of the star as a result of this transit. Otherwise, it is necessary to directly observe the light from the planet.

To be able to directly detect the planet, the extreme contrast between the star light and that of the accompanying planet ($10^{-10}$ for an Earth-like planet around a Sun-like star in the visible wavelength regime) requires the application of a coronagraph, a starshade, or even a space interferometer, to avoid the star from completely drowning out the light from the planet. Future large

*Address all correspondence to Robert Huisman, R.Huisman@SRON.nl

space telescopes, dedicated to direct imaging of exoplanets such as LUVOIR[2] and HABEX,[3] will rely on deformable mirrors (DMs) to achieve clean and stable wavefronts over long periods of time while reducing the negative effect of star light speckles originating from small surface shape errors of the optics. For the DM in such an instrument, this translates to: <1-nm wavefront error correction, shape stability ≤10 pm RMS over 10 s of minutes, high spatial frequency correction ($128 \times 128$ pixels), and extreme reliability.

Currently, the state-of-the-art DMs are developed by Boston Micromachines Corporation (BMC) and AOA Xinetics (AOX). Both have working DMs with $64 \times 64$ pixels. BMC uses MEMS as single electrostatic actuators.[4] They utilize a multiplexer fed by a single high voltage (HV) amplifier to address the different pixels, but the design requires separate wiring for every individual pixel. Another critical issue with this design is that of shape instability as a result of pixel drift. AOX develops both surface-normal and surface-parallel piezoelectric DMs based on lead magnesium niobate (PMN).[5] The AOX DMs are very stable but the discrete nature of the PMN actuators again requires separate wiring for every pixel. It is also difficult to reduce the actuator pitch, which makes application of high pixel number DMs in small imaging systems more difficult. Two $48 \times 48$ pixel AOX DMs are currently baselined for NASA's Wide-Field InfraRed Survey Telescope (WFIRST), scheduled to be launched in the mid 2020s.[6] Other noticeable DM developments, which focus on space applications, are the 44 pixel DM from the University of Münster,[7] the monomorph DM from CILAS,[8] the 57 pixel DM from TNO,[9] and the 24 pixel MADRAS DM.[10] An interesting development making use of radiation pressure as actuation mechanism to address high pixel numbers in a dense configuration is described in Ref. 11. Microscale Inc. specifically addresses the problem of extensive wiring. They have developed lead zirconate titanate (PZT)-based DMs with special ASIC boards to minimize the pixel wiring and reduce the mass of the total system.[12] Finally, a detailed overview of different DM techniques for adaptive optics is provided in Ref. 13.

Scaling of the current state-of-the-art DMs to the needed capabilities for a direct exoplanet imaging space mission is not trivial, in particular concerning the demand on pixel number and pixel density and practical operability (wire bonding, harness, and electronics) in a light weight and reliable design. This paper presents the conceptual design of a hysteretic deformable mirror (HDM), which utilizes large hysteresis in the piezoactuators in combination with an elegant pixel layout to overcome typical problems such as pixel drift and fabrication and reliability of harness and electronics when considering extremely high pixel number and pixel density DMs. We present the principle of operation, the conceptual design, and the current baseline for the fabrication of the hardware. We describe the development of the unique hysteretic piezomaterial, which is of paramount importance for the functioning of the HDM. Furthermore, we provide an advanced strategy to control the shape of the mirror surface. Finally, we discuss critical aspects of the design and provide directions for future research.

## 2 HDM Concept

### 2.1 *Principle of Operation*

Figure 1 shows the conceptual design of the HDM. Deformation of the reflective top layer is realized by a stack of thin piezolayers separated from each other by top and bottom electrodes made of arrays of parallel metallic strips. The strips of the bottom and top electrodes are oriented perpendicular to each other, and they are equally aligned for all layers, in such a way that the bottom electrode strips of the different layers lay directly above each other and are electrically connected, the same being true for the top electrode strips. Single actuator pixels are simply defined by this electrode layout. The electric field, generated when applying a voltage over any two perpendicular strips, causes local deformation of the sandwiched piezolayer at the crossing of those particular electrodes. The simulations that support this idea are presented in Sec. 2.2.

For clarity, only a very limited number of layers are shown in Fig. 1. As for standard piezostack actuators, the required voltage to reach a certain total deformation decreases when more layers with intermediate electrodes are applied. The required number of layers depends on the

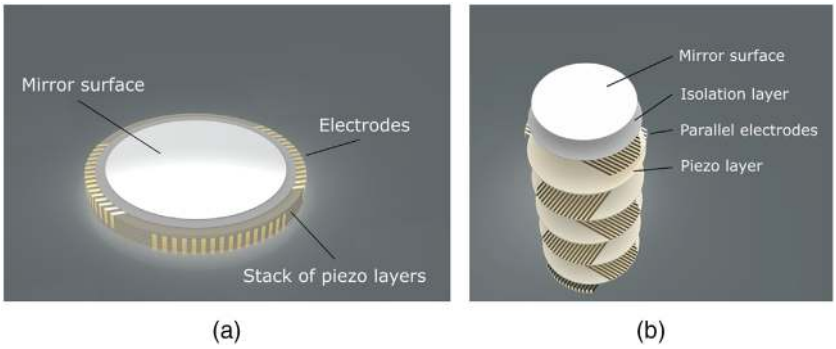


**Fig. 1** (a) HDM conceptual design. (b) Exploded view. Deformation of the mirror is realized by a stack of piezolayers each with perpendicular top and bottom electrodes. Electrode strips that are directly above each other are electrically connected and commanded by a single input voltage. For clarity, only five layers with $16 \times 16$ pixels are shown, the final hardware, however, will consist out of a larger number of these layers with $128 \times 128$ pixels to improve the performance of the DM.

final material properties and thickness of the piezolayers (as discussed in Sec. 4) and the required stroke for the considered application. This is discussed in more detail in Sec. 6.

The application of low voltages (in the order of 10s of Volts) makes it possible to scale down the electrode width and pitch. It also eliminates the need for an HV amplifier. Another advantage is that because of the large ratio between pixel pitch and layer thickness, the electric field ($E$-field) is constrained to a small surface array, limiting the cross talk between the pixels and again facilitating a very compact design.

Figure 2 shows how the single pixels are addressed by the electronics. The use of strip electrodes minimizes the harness to a single wire per electrode. Therefore, the harness scales with the square root of the number of pixels $2\sqrt{n}$, rather than $n$. This reduces the number of separate wires for a $128 \times 128$ pixel DM from 16,384 to 256. We apply time division multiplexing to address the single pixels, which means that we only need a single amplifier instead of $n$ of them.

The use of strip electrodes to define individual pixels can only work when the actuated pixels keep their commanded position after completely removing the locally generated $E$-field. We solved this fundamental problem by developing piezomaterial with an asymmetric/distorted butterfly loop, which functions as a set-and-forget actuator. We have achieved this by means of Niobium doping of piezoelectric PZT, which we call PNZT, as described in more detail in Sec. 4.

It is also this highly nonlinear characteristic of the PNZT material that guarantees that although during actuation of a single pixel shape changes are observed at all crossings along

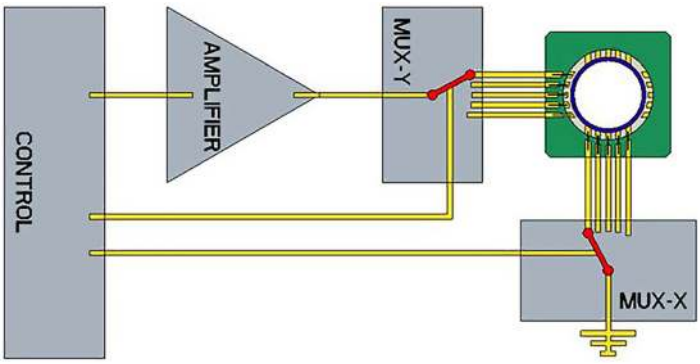


**Fig. 2** HDM system layout. Both the amplifier and the MUXs are set by the control system. All vertically stacked electrodes are interconnected and are addressed by a single input from the amplifier. MUX-X is connected to ground. For clarity, only $5 \times 5$ electrodes are used in this example.

the addressed electrodes (see Sec. 2.2), remnant deformation will only be observed at the commanded pixel location. The details about how this is exploited in the control of the system are provided in Sec. 5.3.

The set-and-forget nature and the application of low voltage input signals greatly reduce the power dissipation of the DM, because no constant HV-input or high update frequency is required to avoid pixel drift as a result of charge leakage of the holding capacitor[14] when high pixel number DMs are considered. This is not only advantageous from an operational point of view but it also limits thermoelastic deformations in the imaging system and eliminates pixel instability as a result of noise in the driver electronics. The limited number of electronic components and wiring, together with the stiff mechanical design of the HDM, guarantees a lightweight and compact system that is very robust to failure and vibration loads. We consider this to be an important merit of the design, as reliability is by far the most important requirement for space applications.

## 2.2 *HDM Pixel Response*

To support the conceptual idea, a finite element analysis (FEA) has been performed that simulates the electric field generation in the piezoelectric array and the resulting pixel response. The simulation considers the $d_{33}$ component of the piezoelectric coefficient. As discussed in Sec. 2.1, when an electric potential is placed on one of the top electrode strips while one of the bottom strips is connected to ground, an electric field is generated in the piezolayers at the crossing of the two strips. This will yield a piezoelectric response and deformation of the respective pixel in all piezolayers.

To simulate the activation of a pixel in a single layer of piezomaterial, the conceptual structure of the HDM was generated in Comsol Multiphysics 5.5 using the Solid Mechanics and Electrostatics modules, i.e., piezoelectric devices multiphysics interface. A 750-nm-thick piezoelectric layer of commercial PZT-5H was created, actuated by five parallel strips as top electrodes and five parallel strips as bottom electrodes, the latter oriented perpendicularly to the top electrode strips, as previously introduced. The width of the single electrodes was set to 1 mm and the pitch between the electrodes (distance from electrode center to electrode center) was 2 mm. We will refer to this configuration as a $5 \times 5$ electrode grid. This grid was modeled using the thin layer boundary condition to define the electrodes in two-dimensional instead of three-dimensional and reduce the computational effort. The outer edges of the model and the bottom boundary were set to be mechanically clamped (modeled by the fixed boundary condition). To activate the center pixel, an electric potential of 2.5 V was applied to the center top strip while the center bottom strip was connected to ground. The surrounding strips were provided with the floating potential condition. Mesh refinement studies were undertaken to ensure convergence of the results. The simulation does not include the exotic hysteretic behavior of the newly developed material, so no remnant deformation is observed.

Figure 3(a) shows the distribution of the electric potential when only addressing the center pixel. The visualization presents a cut through the $xy$-midplane. Due to the fact that certain pixels share either top or bottom electrodes, it is implied that neighboring pixels along a line share the introduced charges on the electrodes that are distributed through the material. From this, it is clear that not only at the intersection of the active strips but also at the other pixel locations along both strips, an electric field is generated. In the following, we will refer to this as electrical coupling. Although the field strength is clearly lower at these offset positions, this will result in deformation of the piezosurface at the mentioned offset positions while the potential difference is applied between the two strips, as can be seen in Fig. 3(b). Figures 3(c) and 3(d) show the simulated deformation when addressing respectively one of the pixels at the outer edge and one of the pixels next to the center pixel. The same characteristic response is observed as for the center pixel. Exploiting the memory introduced by the hysteresis, which is described using a class of Preisach hysteresis operator presented in Refs. 15 and 16, it is possible to determine conditions such that the application of the control signal to every pixel does not modify the remnant deformation of the previously set pixels, therefore, overcoming this potentially limiting effect. This is discussed in more detail in Sec. 5.3.

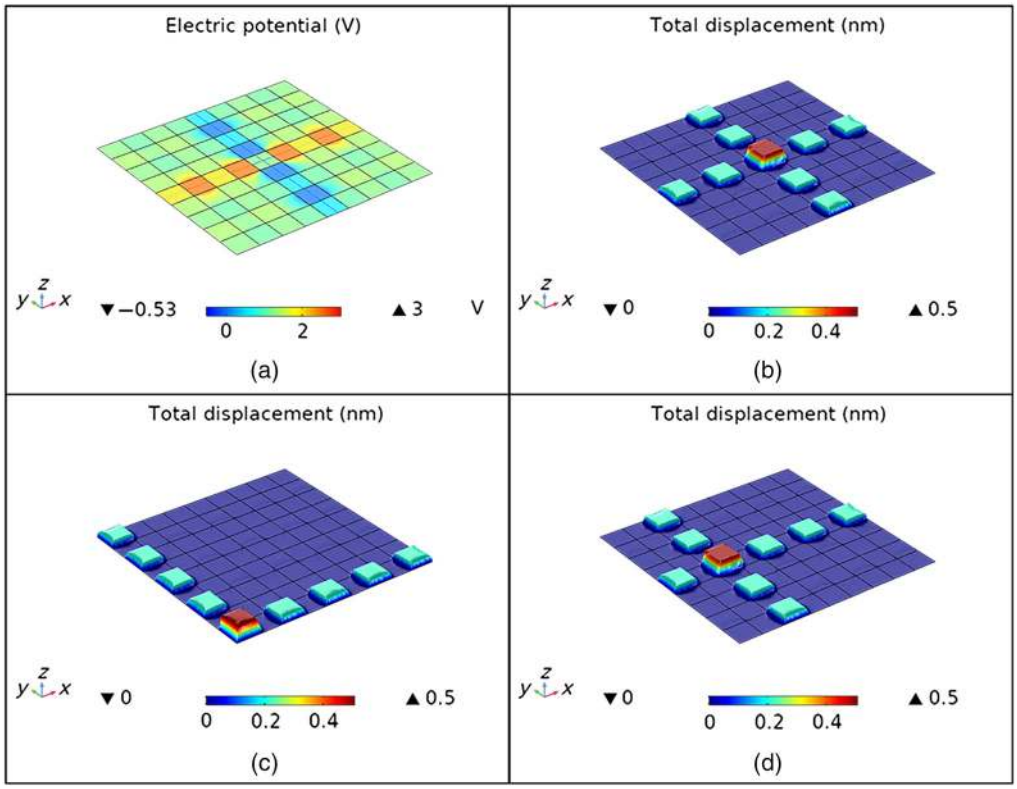


**Fig. 3** FEA of a $5 \times 5$ pixel array. Different electrodes were addressed by applying an electrical potential of 2.5 V on the relevant top strip while the bottom strip was grounded. The strips were modeled by means of the thin layer boundary condition. (a) The distribution of the electric potential in the *xy*-midplane when addressing the center pixel. (b)–(d) Deformation of the surface when addressing the center pixel, one of the outer pixels, and an intermediate pixel.. In all cases, the maximum deformation of the addressed pixel amounts to ~0.5 nm.

## 3 HDM Design and Manufacturing

### 3.1 *HDM Design*

Figure 4 shows the layered structure of the HDM. The basis consists of a highly resistive Si wafer with a thin layer of thermally grown oxide. On top of this, a repeating pattern of the following layers is placed sequentially: an *x*-axis oriented array of parallel metal strips, a thin piezolayer, an array of *y*-axis oriented metal strips, and finally another thin piezolayer. The reflective top layer is electrically isolated from the final layer of *y*-axis oriented strips by a separate isolation layer.

As stated earlier, all metal strips that are oriented along the same axis and are positioned directly above each other are electrically connected. Figure 5 shows the vias that connect the different strips. The reliable connection of the strips is one of the critical process steps in the realization of the HDM, and how this is done is discussed in Sec. 3.2. Standard wire bonding technique is used to connect on-chip smaller bond pads to the bigger bond pads on the printed circuit board (PCB), which is attached to the basis.

### 3.2 *HDM Manufacturing*

In Fig. 6, the current baseline for the fabrication of the HDM is presented. The fabrication starts with a highly resistive Si wafer having 2 $\mu$m thermally grown oxide as shown in Fig. 6(a). This oxide layer prevents a possible short between the bottom metal electrode strips on the carrier wafer. Next, the first layer of platinum (Pt) electrodes (*x*-axis oriented) is patterned onto the thermally grown oxide by employing the lift-off process, as shown in Fig. 6(b). For better adhesion of evaporated Pt to the surface, a thin layer (5 nm) of titanium (Ti) or tantalum (Ta) was

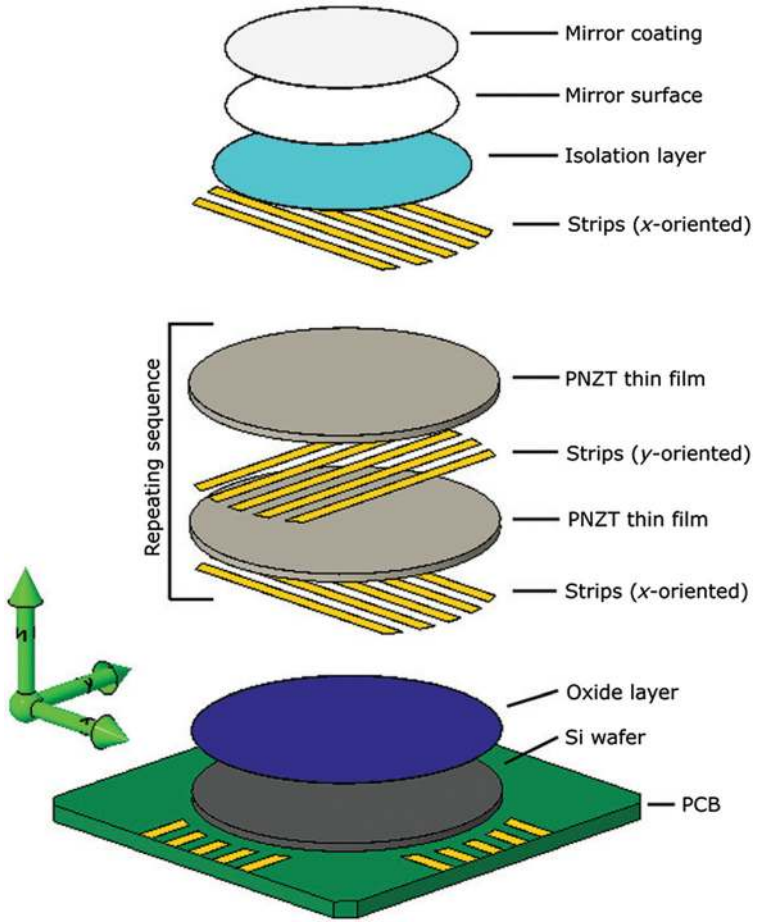


**Fig. 4** HDM layered structure.

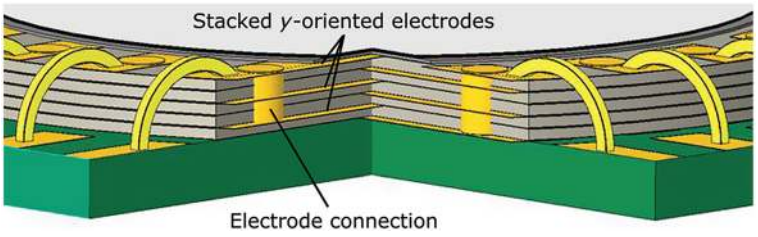


**Fig. 5** Interconnection of metal strips. A cut out of the piezo stack (only five layers in this example) with intermediate metal strip electrodes. The vertical pillars present the connection of all strips that lie directly above each other.

previously deposited on the oxide by evaporation. Our preliminary experiments with metal lift-off using image reversal photoresist and metal evaporation resulted in smooth edges of the metal patterns. This in comparison to the rough edges by sputtered metal. That is why we employ thermally evaporated metals for the lift-off process during the electrodes patterning. The thickness of the Pt layer (usually $\geq$100 nm) and choice of adhesion layer (Ti or Ta) will be such that they can withstand the high temperatures applied during the stacking of sol-gel spin-coated PNZT piezo thin films.

A single PNZT thin film is build up out of approximately ten 100-nm thin nanolayers, which are sequentially deposited by spin coating on top of the $x$-axis oriented electrode strips [Fig. 6(c)]. The $y$-axis oriented Pt strips are then patterned onto the PNZT thin film in a similar way as that of $x$-axis oriented Pt strips by the lift-off process after which the next PNZT thin film is deposited. This sequence is repeated multiple times to produce a stack of PNZT thin films and

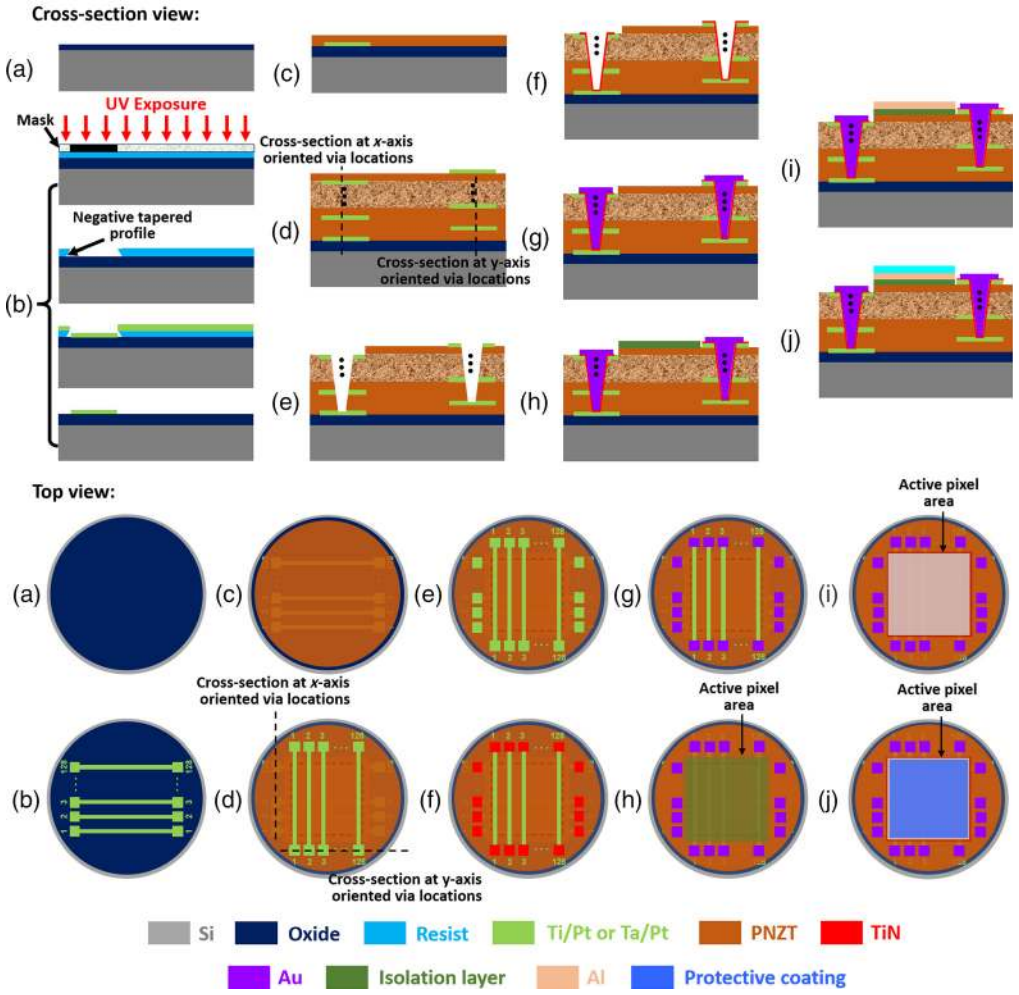


**Fig. 6** Schematic of the baseline process flow for HDM (cross-section and top view). (a) Carrier wafer with 2 $\mu$m thermally grown oxide. (b) Patterning of *x*-axis oriented Pt electrode strips on the oxide. (c) Deposition of PNZT thin film by spin coating. (d) Stacking of PNZT thin films between the *x*-axis and *y*-axis oriented Pt electrodes. (e) RIE of stack of PNZT thin films sandwiched between the *x*-axis and y-axis oriented Pt electrode strips. (f) ALD of TiN thin film to ensure interlayer Pt electrode strip connection. (g) Deposition of Au thin film by evaporation or sputtering for on-chip smaller bond pads. (h) Deposition of insulation layer (polymers, oxides, or nitride) above the active pixel area to have a smooth and flat surface. (i) Deposition of top reflective layer by lift-off using Al evaporation above the active pixel area. (j) Deposition of protective coating by PECVD of ($TiO_2$) above the mirror surface.

Pt electrodes as shown in Fig. 6(d). The alignment of the *x*-axis and *y*-axis oriented Pt electrode strips is done using the alignment markers patterned at the backside of the Si wafer. These back side alignment markers provide a positional accuracy of 1 to 2 $\mu$m during the stacking process. The deposition of the PNZT thin film on the metal strips might result in an uneven topography that needs to be smoothened by means of mechanical planarization, either after each PNZT thin film deposition or once the whole stacking process is completed. This will depend on the evolved topography.

For prototype production, the dry etching technique facilitates etching of vias, at bond pad locations, into the entire PNZT thin films and *x*-axis/*y*-axis oriented Pt electrodes stack, as shown in Fig. 6(e). For interconnection of a large number of electrodes (>10), we prefer wet etching of single thin films in successive steps, before patterning the next *x*-axis/*y*-axis oriented Pt electrodes because of its relatively high etch rate (1.54 $\mu$m/ min)[17] in comparison to dry chemical etching (100 nm/ min).[18] Moreover, wet chemical etching will facilitate expediting the production process, as multiple wafers with PNZT and electrodes stack can be etched

simultaneously. These can then be bonded together to create a large stack of PNZT thin films and electrodes. For our application, the wet etchant needs to be selective toward the mask layer (typically photoresist) that protects the active pixel area and Pt electrodes.

Atomic layer deposition (ALD) can be employed to ascertain interlayer connection of electrodes due to its exceptional conformity on high-aspect ratio structures, independent of the etch profile. These etched vias are conformally covered with a thin titanium nitride (TiN) film (typically few nanometers) [see Fig. 6(f)] to ensure the interconnection of the electrodes in similar orientation. Note that the TiN film by ALD covers the entire wafer; therefore, TiN film needs to be removed from the wafer by a wet etching solution (ammonium hydroxide, hydrogen peroxide, and DI water) while covering the vias with photoresist. Afterward, small on-chip gold (Au) bond pads, as shown in Fig. 6(h), are deposited either by evaporation or sputtering at vias locations. These small bond pads are then connected with the bigger bond pads on the PCB using the wire bonding technique. The wire bonding is the last step in the fabrication line once the deposition of isolation layer, reflective top layer, and protective coating is carried out above the active pixel area, Figs. 6(h)–6(j).

The choice of isolation layer, directly beneath the mirror surface, is primarily based on its ease of processing, low residual stress, adhesion to the underlying interfaces of PNZT/Pt, and its electrical and mechanical properties. It serves to prevent a short with the mirror surface besides providing a flat and smooth surface for top reflective layer deposition. We are currently performing short loop experiments to choose either spin-coated polymers [PDMS, Polyimide (LTC9305) etc.] or plasma-enhanced chemical vapor deposition (PECVD) oxides/nitride ($SiO_2/Si_3N_4$) as isolation layer for the HDM. We are mainly relying on self-leveling[19] properties of the polymers and chemical mechanical planarization of oxides/nitride to have a flat and smooth surface. Moreover, it is required to be able to process the isolation layer at temperatures lower than the maximum thermal budget of the PNZT thin films to avoid inter diffusion of PNZT and platinum, which might degrade the PNZT properties.

For the reflective top layer, aluminum (Al) is the preferred choice due to its high reflectance (>75%) in the visible spectral range for a minimum film thickness of ≥20 nm, irrespective of the underlying isolation layer. Al is selectively deposited by evaporation on top of the flat and smooth isolation layer (right above the active pixel area) using the lift-off process. The choice of Al is not only based on the wavelength range of interest but also on its relatively better oxidation resistance, low residual stress, low surface roughness, adhesion to underlying layer, and ease of processing[20] compared to other potential metals as mirror surface such as silver or gold. Furthermore, a protective coating of dielectric material (such as $TiO_2$) can be applied to prevent the mirror surface from oxidation and scratches while maintaining the high reflectance.

## 4 Development of a Highly Hysteretic Piezomaterial

The term strain memory effect is used to indicate the existence, for some piezoelectric materials, of two stable piezoelectric strain states at zero field that can be accessed through the application of a specific voltage cycle. This corresponds to the display of a shifted strain–electric field (*S*-*E*) loop (also known as butterfly loop), which is asymmetric with respect to the piezoelectric strain axis. Figure 7 shows typical *P*-*E* and *S*-*E* loops of a piezoelectric PZT ceramic. The relation between applied electric field and the induced displacement is highly nonlinear but a negligible remnant deformation is observed after removing the field.

The developed material is based on the well-known family of PZT (the trade name for lead zirconate titanate or $PbZr_{1-x}Ti_xO_3$) with composition close to the so-called morphotropic phase boundary (MPB), which is the Zr/Ti ratio at which a phase transition takes place between a tetragonal and a rhombohedral ferroelectric phase (for $x$0.48). The MPB compositions are those for which the best piezoelectric parameters and electromechanical coupling factors are found. Other properties are tailored through compositional modification and chemical doping to optimize the hysteretic piezoelectric actuators. In particular, we have synthesized a promising candidate for the fabrication of the set-and-forget actuator, namely $Pb(Zr_{0.52}Ti_{0.48})_{0.96}Nb_{0.04}O_2$ with zirconia microparticles, which has been called PNZT. This material exhibits a large longitudinal piezoelectric parameter and stability to fatigue. Furthermore, the strain memory effect has been observed and good mechanical properties have been obtained due to the addition of $ZrO_2$ particles.

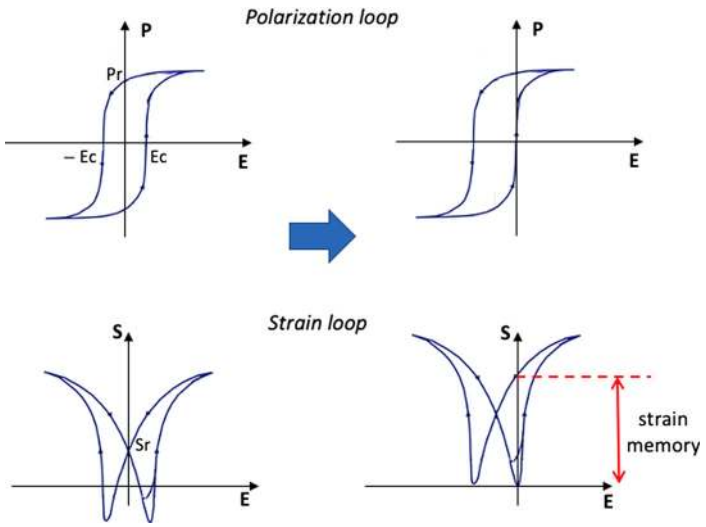


**Fig. 7** Typical polarization and strain loops of high-strain piezoelectric ceramics, such as PZT (left) are compared with those showing strain memory effect (right).

The piezoelectric pellets are composed of a Ti-rich, Nb-doped PZT (PNZT) matrix with embedded $ZrO_2$ microparticles. The presence of niobium and $ZrO_2$ particles in the PNZT matrix influences the piezoelectric response and the mechanical properties by lowering the switching fields and enhancing the piezoelectric coefficient $d_{33}$ and the piezoelectric voltage constant $g_{33}$.[21–23] Niobium ($Nb^{5+}$) as a soft dopant has been selected to increase the piezoelectric coefficients and produce large remnant polarization. Moreover, it has been reported that $Nb^{5+}$ induces the memory effect by producing a horizontal shift in the *S-E* loop, making the butterfly loop asymmetric with respect to the piezoelectric strain axis, due to the presence of an internal bias field.[24]

The conventional mixed oxide route has been used to fabricate PNZT pellets and the precursors are high purity powders of PbO (99.999%), $ZrO_2$ (99.8%), $TiO_2$ (99.6%), and $Nb_2O_5$ (99.99%). The precursors were mixed in stoichiometric amounts with 4% excess PbO to compensate for lead loss during sintering. Afterward, the pellets were shaped with diameters of 5 and 10 mm and with thickness between 0.5 and 1 mm. Then, the samples were sintered at high temperatures. After the sintering process, the samples were poled and the crystal structure and topography was investigated by x-ray diffraction and scanning electron microscopy. The piezoelectric properties were studied using a state-of-the-art ferroelectric/piezoelectric system from aixACCT. As shown in Fig. 8, the samples exhibit a large piezoelectric deformation, with a

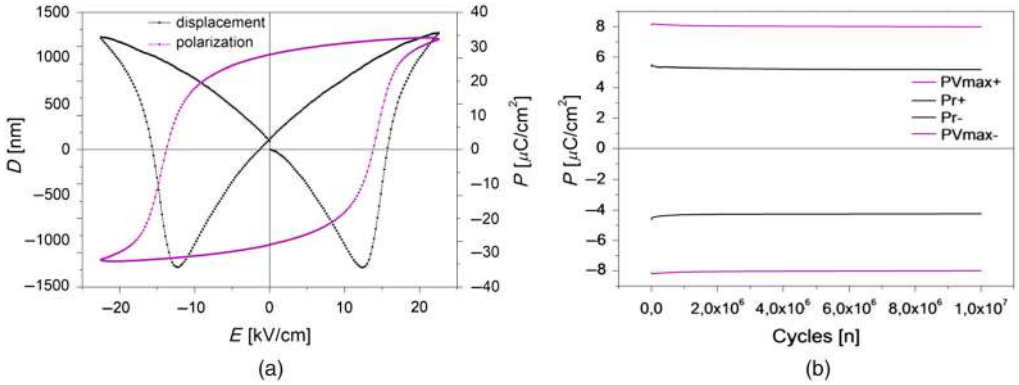


**Fig. 8** Piezoelectric properties of PNZT hysteretic pellet under bipolar electric fields: (a) ferroelectric loops, strain (black), and polarization (purple) as function of applied high electric field at 0.5 Hz and (b) fatigue response showing the maximum ($PV_{max}$ in purple) and remnant ($P_r$ in black) polarization values at electric field cycles of ~15 kV/cm and 1 Hz frequency.

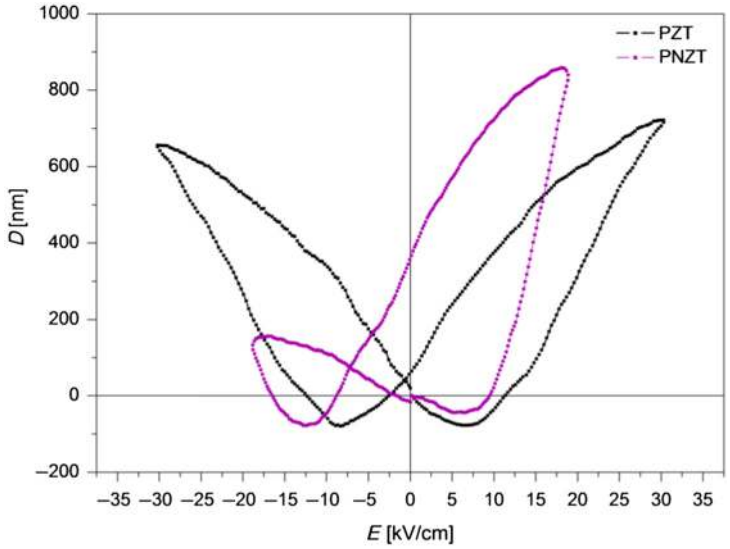


**Fig. 9** Measured strain-electric field (*S*-*E*) loops of PZT (black) and PNZT (purple) pellets at 0.5 Hz. For PNZT, a maximum remnant deformation of ∼400 nm is observed, which is more than 40% of the maximum deformation of the material.

maximum displacement of 1.2 $\mu$m at a field of 20 kV/cm at 0.5 Hz, when the material is fully polarized and its maximum piezoelectric deformation has been reached. This corresponds to an effective piezoelectric $d_{33}$-coefficient of up to 1200 pm/V [Fig. 8(a)]. The samples were also subjected to a fatigue test of at least $10^7$ cycles at electric field cycles of ∼15 kV/cm and 1 Hz frequency [Fig. 8(b)]. The fatigue measurements were repeated with different samples, and they all proved to have good stability to fatigue with almost no change in the maximum ($PV_{max}$) and remnant ($P_r$) polarization after the voltage application.[25]

Figure 9 shows a comparison between the asymmetric *S*-*E* loop of undoped morphotropic PZT and that of the newly developed piezoelectric material PNZT at weak *E*-fields. As longitudinal piezoelectric actuators, the electric field is applied in the sample parallel to the direction of polarization inducing a controlled displacement. For the PNZT sample, a large remnant deformation is present after *E*-field cycling and the amount of remnant deformation can be controlled by the amplitude of the applied field. We observe 40% remnant deformation and the values remain stable after fatigue measurements,[25] which is sufficient for the implementation of multiplexing and allows for a significant reduction of the device power consumption.

## 5 Mechanical Modeling and Control of the HDM

### 5.1 *Modeling of Highly Hysteretic Piezoactuator*

In the literature, the phenomenon of hysteresis has been widely studied and there exist different approaches to describe it mathematically.[26] Despite its mathematical complexity, when it comes to practical applications, the Preisach hysteresis operator has been the preferred mathematical model due to its suitability to describe the hysteresis of different physical phenomena.[27,28]

To describe the hysteresis present in the relation between the electric field and strain/stress of the HDM piezoactuators', we have adopted a modified version of the Preisach hysteresis operator, whose weighting function parameter is allowed to have positive and negative values with a particular distribution.[15,16] This class of Preisach hysteresis operator is able to describe the so-called butterfly hysteresis loops that are experimentally observed in samples of the piezoelectric material used in the HDM as presented in Sec. 4.

Figure 10 shows the fitting result of the Preisach model parameters to the experimentally obtained PNZT *S*-*E* loop. Based on this fit, remnant shape changes can be predicted over the complete operational range of the actuator, with an accuracy of ∼90%.

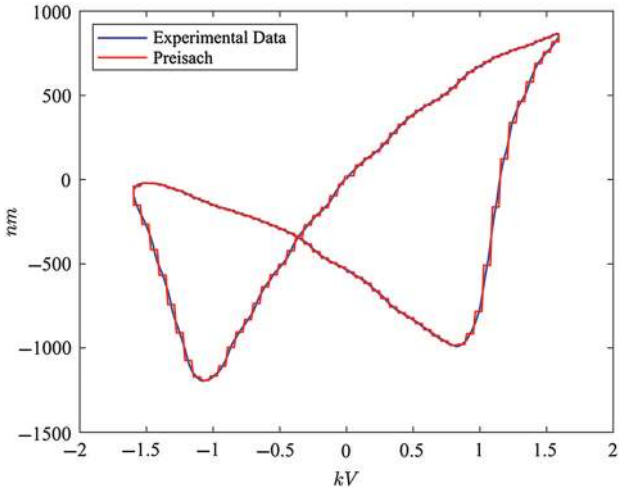


**Fig. 10** Preisach fitting result. The experimental data were obtained using a different PNZT pellet as the results presented in Fig. 9.

## 5.2 *Facesheet Modeling as Input to Control*

In Ref. 29, we describe the calculation of influence functions for the HDM by a detailed consideration of pixel shape, position, and reflective top layer. The developed semianalytical model determines the reference pressure for every single pixel, which serves as valuable input for the controller described in Sec. 5.3. Note that the electrical coupling between the actuators, as described in Sec. 2.2, was not considered in this model, and this is, however, tackled by the control strategy. The modeling approach is summarized in the following.

To describe the shape changes of the reflective top layer, we considered the Poisson equation[30] in polar coordinates, governing the relation between small surface displacements of the thin top layer and surface tension generated by the pixels. Incorporating the HDM's particular arrangement of the electrodes into the solution to Poisson's equation provides the deformation of the reflective top layer at a specific surface point. To include the mechanical behavior of the actuators, each actuator was modeled as a spring in parallel to a force source. The pressure exerted by the actuators at a specific position on the mirror surface comprises two components: a stiffness and force source over an area. Based on this implementation, the input for the Preisach hysteresis model, used to control the shape of the mirror, can be independently determined.

In Ref. 29, we present detailed simulation results on the fitting of the mirror surface to low- and higher-order Zernike polynomials, a preferred representation for optical wavefront aberations. The optimal pressure for each actuator was calculated by solving an overdetermined set of equations in the least-square sense, minimizing the root-mean-square deviation between actual and desired shape.

## 5.3 *Control Strategy*

For the design of an HDM control strategy, a simplified model of the electrically coupled actuators as shown in Fig. 11 is considered. In this model, each actuator force source component is modeled by a Preisach operator $\Phi_i$ whose input corresponds to the electric field present in the same actuator. In addition, two signals are considered: a control signal $\nu$ whose value corresponds to the electric field applied to the electrodes and a switching signal $\sigma$ whose value indicates the actuator to which the electric field control signal is directly being applied. The effects of the electric coupling are captured by the factors $\lambda_{i,j}$, whose values are always less than one. Thus, when the switching signal indicates that the actuator $i$ is selected, the control signal $\nu$ is directly applied to the actuator $i$ and the other actuators receive an attenuated version of the control signal $\nu$ scaled by the factors $\lambda_{*,i}$.

Based on this model and using the optimal pressure computed for each actuator as a reference (see Sec. 5.2), a control loop is proposed to sequentially drive the actuators of the HDM to their

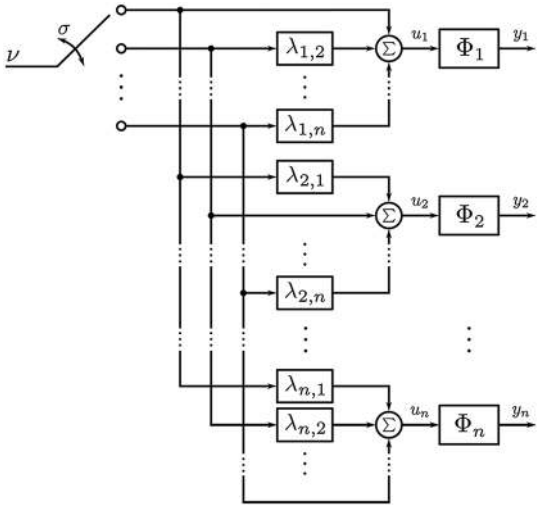


**Fig. 11** Simplified model of the electrically coupled actuators used in the control strategy of the HDM. $\Phi_i$ are the Preisach operators, $\lambda_{i,j}$ are the electric coupling factors, $\nu$ is the control signal, and $\sigma$ is the switching signal.

reference value. The strategy to control the complete HDM is inspired by the iterative learning control methodology and based on the work introduced in Ref. 31, which addresses the problem of driving the remnant of a single hysteretic actuator whose behavior can be described by a Preisach operator. In the case of the HDM, the proposed control algorithm is presented in Algorithm 1. This algorithm relies on the possibility to set all the actuators of the mirror to a known initial state applying a predefined initialization signal to all of them at the same time and exploiting the so-called consistency property of hysteresis and the Preisach operator to disregard the effect of the electrical coupling when the input amplitudes are within an allowed range depending on the coupling factors $\lambda_{i,j}$. Roughly speaking, to set the HDM to a certain configuration, it is considered that an initialization signal is applied to all the actuators at the same time and posteriorly an iteration of the control loop can run where the switching signal selects each

**Algorithm 1** HDM control algorithm

**Input:** Number of actuators: $n_a$, pressure reference vector: $y^{\text{ref}}$, error threshold: $e^{\text{threshold}}$, update gain: $\gamma$

**Init:** set amplitudes: $w_i = 0$ for all $i \in \{1 \dots n_a\}$

**while** not($e_i < e^{\text{threshold}}$ for all $i \in \{1 \dots n_a\}$) **do**

  apply initialization signal to all actuators

  obtain indexes of ascending sorted amplitudes:

    $idxs$ = index_ascending_sorted(vector $= w$)

  **for** $j = idxs$ **do**

    set switching signal: $\sigma = j$

    apply input: $\nu$ = triangle_pulse(amplitude = $w_j$)

    compute error: $e_j = y_j - y_j^{\text{ref}}$

    update amplitude: $w_j = w_j + \gamma \cdot e_j$

  **end**

**end**

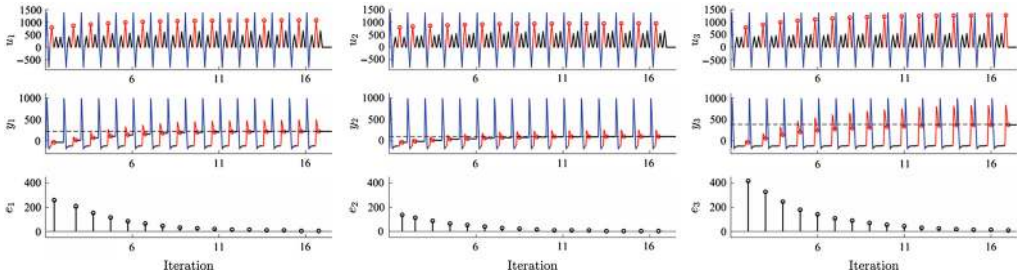


**Fig. 12** Simulation of the first 17 iterations of Algorithm 1 for three electrically coupled identical actuators in HDM. From left to right, each figure corresponds to the closed-loop behavior of one actuator system that is placed according to the same sequence found in these subfigures. At each subfigure, the input $u_i$ is at the top with the triangular pulse amplitudes $w_i$ at every iteration marked by a red circle, the corresponding pressure output $y_i$ is in the middle with the remnant pressure at every iteration marked also by a red circle, and the reference value $y_i^{\text{ref}}$ indicated by a dashed line, and the corresponding error $e_i$ after every iteration is at the bottom. The blue segments of the inputs and outputs indicate the periods when the initialization signal is applied to all actuators and the red segments indicate the periods when the switching signal $\sigma$ selects the corresponding actuator and the control signal $\nu$ is directly applied (i.e., $\sigma = i$ and $u_i = \nu$). It can be observed that when the control input is directly applied to one actuator, the other two receive a 50% attenuated version of it indicated by the black segments of the inputs, and that the remnant of each actuator is close enough to its reference value after the last iteration of the algorithm when inputs are set permanently to zero (i.e., $u_i = 0$).

actuator of the HDM once for a predefined period of time. During this period, the selected actuator receives a control signal consisting of a triangular pulse whose amplitude is computed based on the error between its corresponding reference value and the actual pressure of the actuator at the previous iteration. Correspondingly, due to the effect of the electric coupling, the neighboring actuators receive an attenuated version of the triangular pulse within the same time period. When our proposed iterative control algorithm is applied to each pixel, the effect of this attenuated pulse to the neighboring pixels can be avoided by *a priori* determining the actuators' update sequence in the ascending order of magnitude of the triangular pulse to be applied. The iterations of the control loop are repeated until for every single pixel the appropriate pulse amplitude is found and the desired surface shape is achieved.

To validate the working principle of the proposed control strategy, a simulation of three coupled actuators described by the model of Fig. 11 was performed. For illustration purposes, during the simulation it was assumed that the pressure output of the actuators can be known based on their position and the influence functions obtained from the semianalytical surface model as described in Sec. 5.2. However, for further developments, the algorithm will be modified and estimations of the actual pressure in each actuator will be obtained based on the measurements of the actual influence functions of the mirror surface. The parameters for the simulation were set as follows. The reference values of the actuators were set to 220 nm for actuator 1, 100 nm for actuator 2, and 380 nm for actuator 3. All coupling factors $\lambda_{i,j}$ were set to 0.5. The initial pulses amplitudes for the three actuators were set to 800 V and the gain used for the pulse amplitude update at every iteration was $\gamma = 0.28$. The results are presented in Fig. 12. The control loop is truncated after the first 17 iterations and after the input of the three actuators is set permanently to zero. From the bottom plots of each subfigure, it can be appreciated that the error is negligible and the remnant of each actuator is close enough to its reference value marked at the middle plots of each subfigure by black dashed lines.

## 6 Discussion

Prior to the development of the HDM, as described in Sec. 2, a proof of concept will be manufactured using a single thick ceramic pellet of PNZT. This pressed PNZT pellet will have a diameter of 10 mm, a thickness between 100 and 500 $\mu$m, and a $5 \times 5$ electrode layout. The final HDM will be build up out of a large stack of PNZT thin films. Apart from the already

discussed advantages of the use of thin layers of piezomaterial, the high homogeneity of these thin films guarantees identical pixel response over the complete mirror surface.

For the production of the PNZT thin films, we are developing a chemical solution that enables the deposition of multiple nanolayers of the PNZT material by the process of spin coating.[32,33] This technique has been chosen because it allows for the preparation of thicker (1 to 10 $\mu$m) and very homogeneous thin films with large diameter, which facilitates the transition to large-scale industrial applications. Early results presented in Ref. 33 show a maximum deformation of 0.3% of the total film thickness,[33] which corresponds to the values found in the literature.[34,35] A slight shift of the ferroelectric strain loop is observed, which indicates the presence of an internal bias field, that suggests a small remnant deformation. However, further research is needed to get the desirable memory effect of the film and required maximum deformation for our DM application. In particular, the multilayered deposition technique demands optimization to increase the homogeneity and quality of the films. A more detailed study of the effects of $Nb^{5+}$ as a soft dopant in thin films is needed, as the piezoelectric properties can also be affected by the raw materials and fabrication process. Thus, the composition used for the fabrication of PNZT bulk is not necessarily identical to that of the thin films. Moreover, incorporation of the $ZrO_2$ microparticles into the (multilayered) PNZT thin film is still in progress.

The extreme DM requirements, applicable to the direct detection of exoplanets, in combination with the limitations imposed by both the space craft and the harsh space environment, form a substantial challenge for the hardware development. These demand the use of large stacks of the PNZT thin films to be able to meet functional specs of low voltage and high pixel density and to optimize performance.

When we limit the allowed deformation to 0.1% of its total thickness, for 10-$\mu$m thick thin films a stack of 250 layers would be required to reach a maximum deformation of 1 $\mu$m (considering 40% remnant deformation). To limit the number of independent piezolayers, an important focus of the PNZT thin film development will be on the realization of relatively thick PNZT thin films. Another approach we are currently investigating is the development of so-called "composite PNZT" with a mixture of chemical solution with fillers such as PNZT microparticles. The aim of this study is to produce 10-to 100-$\mu$m thick PNZT layers with still sufficient homogeneity. Apart from this, we are working on automation of parts of the process. This not only makes the production of large amounts of thin films possible but also improves the process control, which is critical for the quality of the final product.

The Comsol model, presented in Sec. 2.2, illustrates the electrical coupling between the pixels arising from the electrode layout and electrical field distribution. This was shown by generating a simplified model that does not make use of the newly developed piezoelectric material, which is not available in any material libraries. We have therefore used PZT-5H as a basis material and presented a purely stationary analysis. To support the final design of the HDM, current research is focusing on a more complex finite element model including the characteristics of the memory material, the proposed electrode layout, the isolation layer, and mirror surface on top of the base structure in a time-dependet study. This model could be used to optimize the proposed design and simulate the operation of the HDM.

The PNZT actuator shows similarity to the PI-rest actuator[36] recently developed by Physik Instrumente (PI) GmbH & Co. Remnant deformation of this piezoactuator can be controlled by changing the polarization state of the material. PI-rest is manufactured using multilayer piezoactuators and its active material is soft PZT ceramics. Soft PZT ceramics are characterized by a large piezoelectric constant and good electromechanical coupling factors but also by low mechanical quality factors, easy depolarization, and poor linearity.[37,38] Although the PNZT actuator is fabricated using Nb as a soft dopant, the produced PNZT material with $ZrO_2$ particles exhibits good mechanical properties, linearity, and good resistance to fatigue and depolarization. Nevertheless, the most distinguish characteristics of PNZT actuators are: (1) fabrication of the device with high actuator number (pixels), which reduces the power consumption and simplifies the electronics and control of the system and (2) the development of thin films (in addition to pellets) for large-scale surface actuators and reduction of the input voltage, which also reduces the overall fabrication cost of the DM.

The time required for a single shape correction of the mirror is mainly dependent on the speed with which single pixels can be set. With the extremely large number of pixels and the iterative

nature of the control strategy, a single shape correction might take hours to complete. Currently, the limiting factor seems to be the material properties of the PNZT, which limits the speed with which the triangular voltage input can be applied to address a single pixel. Future material research will focus on ways to improve this response speed of the material.

With our development, we focus on space-based DMs where small stroke but highly accurate corrections for static (imperfections) and slowly moving (thermal) aberrations are required. We strongly believe, however, that the concept has wide spin off possibilities in the high tech industry such as chip manufacturing, high intensity lasers, and microscopy. For these applications, we are not only considering the application as DM but also as deformable surface or as single set and forget actuator. As these applications are typically less restrictive in operational conditions (e.g., applied voltage, vacuum conditions, stroke) also, the option of PNZT hybrids or even pellets can be considered here. The valuable knowledge gained in this study can directly be put to use when considering these other applications.

## 7 Conclusions

We have introduced the HDM concept and provided an overview of the critical technology steps for the realization of the hardware. The concept, to produce very high pixel numbers in a dense configuration by the application of a simple electrode layout, is supported by FEA of the electric field propagation and deformation of a single layer of standard PZT material. The control strategy accounts for the observed deformation of the neighboring pixels and brings the mirror to its final shape in an iterative process. Both the pixel addressability and the use of time division multiplexing (TDM) rely on the development of piezomaterials with large remnant deformation. Efforts have been devoted to develop such a material and here we show our progress in this direction presenting a PZT-based composite ceramic that exhibits 40% remnant deformation, which is sufficient to serve as set-and-forget actuator.

Our aim is to develop a pellet-based demonstrator. This $5 \times 5$ pixel DM will serve as proof of principle and should validate the concept of single pixel addressing by TDM in combination with the simple electrode layout. It should also verify that the set-and-forget nature of the PNZT results in stable shape configurations without the need for constant actuation or a high update frequency and the ability to shape the mirror by application of the developed control strategy. In parallel, we will work on the further development of the material, the control, and the fabrication steps involved with the production and operation of a final HDM.

## Acknowledgments

The authors would like to thank C. de Jonge for his conceptual work on the HDM design, W. van de Beek for his contribution to the development of the HDM Preisach operator, V. Murugesan for his support with the short loop experiments, and J. Baas and H. Bonder for their technical support. This work was cofunded through a Marie Sklodowska-Curie COFUND (DSSC 754315), a NSO/NWO PIPP grant, and a FOM/f Fellowship of the Dutch Research Council (NWO). The authors declare no conflicts of interest.

## References

1. J. Wright and B. Gaudi, "Exoplanet detection methods," in *Planets, Stars and Stellar Systems*, T. D. Oswalt, L. M. French, and P. Kalas, Eds., pp. 489–540, Springer, Dordrecht (2013).
2. The LUVOIR Team, "The LUVOIR mission concept study final report," https://asd.gsfc.nasa.gov/luvoir/reports/ (2019).
3. B. S. Gaudi et al., "The habitable exoplanet observatory (HabEx) mission concept study final report," https://arxiv.org/abs/2001.06683 (2020).
4. T. Bifano, "MEMS deformable mirrors," *Nat. Photonics* **5**(1), 21–23 (2011).
5. A. Wirth et al., "Deformable mirror technologies at AOA xinetics," *Proc. SPIE* **8780**, 87800M (2013).

6. D. Spergel et al., "Wide-field infrarred survey telescope-astrophysics focused telescope assets WFIRST-AFTA 2015 report," arXiv: 1503.03757 (2015).
7. P. Rausch, S. Verpoort, and U. Wittrock, "Unimorph deformable mirror for space telescopes: environmental testing," *Opt. Express* **24**, 1528–1542 (2016).
8. R. Cousty et al., "Monomorph deformable mirrors: from ground-based facilities to space telescopes," *Proc. SPIE* **10562**, 1056231 (2017).
9. S. Kuiper et al., "Electromagnetic deformable mirror development at TNO," *Proc. SPIE* **9912**, 991204 (2016).
10. M. Laslandes et al., "Last results of MADRAS, a space active optics demonstrator," *Proc. SPIE* **10564**, 1056413 (2017).
11. P. Riaud, "New high-density deformable mirrors for high-contrast imaging," *Astron. Astrophys.* **545**, A25 (2012).
12. C. M. Prada et al., "Characterization of low-mass deformable mirrors and ASIC drivers for high-contrast imaging," *Proc. SPIE* **10400**, 1040011 (2017).
13. P. Y. Madec, "Overview of deformable mirror technologies for adaptive optics and astronomy," *Proc. SPIE* **8447**, 844705 (2012).
14. M. N. Horenstein et al., "Ultra-low-power multiplexed electronic driver for high resolution deformable mirror systems," *Proc. SPIE* **7930**, 79300M (2011).
15. B. Jayawardhana et al., "Modeling and analysis of butterfly loops via Preisach operators and its application in a piezoelectric material," in *IEEE Conf. Decision and Control*, pp. 6894–6899 (2018).
16. M. A. Vasquez-Beltran, B. Jayawardhana, and R. Peletier, "On the characterization of butterfly and multi-loop hysteresis behavior," arXiv: 2012.03605 (2020).
17. H. Wang et al., "A one-step residue-free wet etching process of ceramic PZT for piezoelectric transducers," *Sens. Actuators A* **290**, 130–136 (2019).
18. M. Bale and R. Palmer, "Deep plasma etching of piezoelectric PZT with $SF_6$," *J. Vacuum Sci. Technol. B* **19**(6), 2020–2025 (2001).
19. C. Rawlings et al., "Accurate location and manipulation of nanoscaled objects buried under spin-coated films," *ACS Nano* **9**(6), 6188–6195 (2015).
20. G. Totten and D. MacKenzie, *Handbook of Aluminum, Vol. 1: Physical Metallurgy and Processes*, CRC Press, Boca Raton (2003).
21. A. Benčan et al., "Structure and the electrical properties of $Pb(Zr,Ti)O_3$—Zirconia composites," *J. Am. Ceram. Soc.* **95**(2), 651–657 (2012).
22. M. D. Nguyen et al., "Effect of dopants on ferroelectric and piezoelectric properties of lead zirconate titanate thin films on Si substrates," *Ceram. Int.* **40**(1), 1013–1018 (2014).
23. S.-Y. Chu et al., "Doping effects of Nb additives on the piezoelectric and dielectric properties of PZT ceramics and its application on SAW device," *Sens. Actuators A* **113**(2), 198–203 (2004).
24. R. D. Klissurska et al., "Use of ferroelectric hysteresis parameters for evaluation of niobium effects in lead zirconate titanate thin films," *J. Am. Ceram. Soc.* **80**(2), 336–342 (1997).
25. S. Damerio, "Synthesis and implementation of piezoelectric materials as actuators for hysteretic deformable mirrors," Master Thesis, University of Groningen (2017).
26. F. Preisach, "Über die magnetische Nachwirkung," *Z. Phys.* **94**(5), 277–302 (1935).
27. V. Hassani, T. Tjahjowidodo, and T. N. Do, "A survey on hysteresis modeling, identification and control," *Mech. Syst. Sig. Process.* **49**(1–2), 209–233 (2014).
28. G. Gu et al., "Modeling and control of piezo-actuated nanopositioning stages: a survey," *IEEE Trans. Autom. Sci. Eng.* **13**(1), 313–332 (2016).
29. A. E. M. Schmerbauch et al., "Influence functions for a hysteretic deformable mirror with a high-density 2D array of actuators," *Appl. Opt.* **59**, 8077–8088 (2020).
30. P. M. Morse and H. Feshbach, *Methods of Theoretical Physics, Part II*, McGraw-Hill, New York (1953).
31. M. A. Vasquez-Beltran, B. Jayawardhana, and R. Peletier, "Recursive algorithm for the control of output remnant of Preisach hysteresis operator," *IEEE Control Syst. Lett.* **5**(3), 1061–1066 (2021).
32. E. van der Veer, "Sol-gel synthesis of piezoelectric materials for deformable mirror applications," Master Thesis, University of Groningen (2019).

33. E. van der Veer, M. Acuautla, and B. Noheda, "Ferroelectric $PbZr_{1-x}Ti_xO_3$ by ethylene glycol-based chemical solution synthesis," arXiv: 2007:11694 (2020).
34. D. Balma et al., "High piezoelectric longitudinal coefficients in sol–gel PZT thin film multilayers," *J. Am. Ceram. Soc.* **97**(7), 2069–2075 (2014).
35. R. D. Klissurska et al., "Effect of Nb doping on the microstructure of sol–gel-derived PZT thin films," *J. Am. Ceram. Soc.* **78**(6), 1513–1520 (1995).
36. J. Reiser and H. Marth, "PIRest technology: how to keep the last position of PZT actuators without electrical power," in *16th Int. Conf. New Actuators*, pp. 1–4 (2018).
37. J. Holterman and P. Groen, *An Introduction to Piezoelectric Materials and Applications*, Stichting Applied Piezo, Apeldoorn (2013).
38. B. W. Lee and E. J. Lee, "Effects of complex doping on microstructural and electrical properties of PZT ceramics," *J. Electroceram.* **17**(2–4), 597–602 (2006).

**Robert Huisman** received his BS degree in mechanical engineering from Hanze Hogeschool Groningen, Groningen, The Netherlands, in 1996. He received his MS degree in astronomy in 2001 and his PhD in control theory in 2016, both from the University of Groningen, Groningen, The Netherlands. Since 2001, he has been with the Netherlands Institute for Space Research, where he is working as an instrument scientist. He is currently leading the development of the hysteretic deformable mirrors (HDM).

**Marcel P. Bruijn** studied experimental physics at the University of Amsterdam. In 1986, he finished his thesis on multilayer x-ray reflection coatings. Shortly hereafter, he became head of the microlithography section at Space Research Organization Netherlands (SRON)-Utrecht. Over the years, he has worked on many R&D projects in the area of cryogenic detectors for astronomy. He developed high-Q superconducting readout elements for cryogenic detectors. He is the author of 36 and coauthor of more than 150 publications.

**Silvia Damerio** received her BS degree in chemistry from the University of Genova, Italy, in 2015, and her MS degree in chemistry from the University of Groningen, the Netherlands, in 2017. She worked on the HDM project as part of her MS research project. She is now conducting her PhD in materials science at Zernike Institute for Advanced Materials of the University of Groningen.

**Martin Eggens** received his BSc degrees in mechanical and electrical engineering from Hogeschool Drenthe, Emmen, The Netherlands, in 1995 and 1997. Since then, he has been a senior mechanical design engineer at SRON, Groningen, The Netherlands. He is mainly involved in engineering of optomechanical design, analysis (vibration, thermal), and mechanisms of cryogenic space instrumentation such as ESA/Herschel/HIFI and ground equipment. As mechanical lead engineer, he was involved in the development of SAFARI instrument for the ESA/JAXA/SPICA mission.

**Syed N. R. Kazmi** is an instrument scientist at SRON responsible for the process flow development to fabricate HDM for space applications. He received his MSc degree in physics from Quaid-I-Azam University, Islamabad, Pakistan, and his MS leading to PhD in microsystems from the University of Twente, Enschede, The Netherlands.

**Anja E. M. Schmerbauch** received her BSc and MSc degrees in mechanical engineering from Ilmenau University of Technology, Ilmenau, Germany, in 2016 and 2017, respectively. She is currently working as a PhD student within the research group of Discrete Technology and Production Automation, Faculty of Science and Engineering, University of Groningen, The Netherlands.

**Heino Smit** has been working at SRON for over 25 years as an electrical design engineer. His main contributions were on the Herschel HIFI space telescope and the SPICA Safari instrument. At the moment, he is working on a space simulator for testing the camera's of the PLATO instrument. For the HDM project, he is responsible for the general electronics, the amplifiers, and the TDM.

**Marco Augusto Vasquez-Beltran** received his BSc degree in electronics engineering from the Instituto Tecnologico de Orizaba, Orizaba, Mexico, in 2013, and his MSc degree in electrical engineering from the Centro de Investigación y de Estudios Avanzados (CINVESTAV), Mexico, Mexico, in 2015. He is currently a PhD graduate student at the University of Groningen, Groningen, The Netherlands.

**Ewout van der Veer** received his BSc and MSc degrees in chemistry from the University of Groningen, the Netherlands, specializing in materials chemistry. He is now pursuing a PhD at the Zernike Institute for Advanced Materials, University of Groningen, under the supervision of Professor Beatriz Noheda, working on ferroelectric lithography for electronics applications.

**Mónica Acuautla** received her BS degree in mechatronics and her PhD in micro/nanoelectronics. Now, she is a tenure-track assistant professor leading the group of Engineering Materials for Mechanical Systems at the University of Groningen. Her research aims at the design and fabrication of piezoelectric and mechatronic devices, piezoelectric energy harvesting, synthesis and characterization of ferroelectric and piezoelectric materials, MEMS/NEMS, flexible electronics, sensors and actuators.

**Bayu Jayawardhana** received his PhD in electrical and electronics engineering from Imperial College London, U.K. He is a professor of mechatronics and control of nonlinear systems in the Faculty of Science and Engineering, University of Groningen, The Netherlands.

**Beatriz Noheda** received her BS, MS, and PhD degrees in physics from the University Autonoma in Madrid. She is currently full professor at the Zernike Institute for Advanced Materials, University of Groningen, and the founding director of the Groningen Cognitive Systems and Materials center (CogniGron). She is a fellow of the American Physical Society and recipient of the IEEE- Robert E. Newnham Ferroelectrics Award. She has served in numerous committees and several editorial boards.